Dynamics of single-wall carbon nanotube synthesis by laser vaporization

A.A. Puretzky, D.B. Geohegan, X. Fan, S.J. Pennycook

Solid State Division, Oak Ridge National Laboratory, P.O. Box 2008, Oak Ridge, Tennessee 37831-6056, USA
(Fax: +1-423/576-3676)

Abstract. The key spatial and temporal scales for single-wall carbon nanotube (SWNT) synthesis by laser vaporization at high temperatures are investigated with laser-induced luminescence imaging and spectroscopy. Graphite/(Ni, Co) targets are ablated under typical synthesis conditions with a Nd:YAG laser at 1000 °C in a 2-in. quartz tube reactor in flowing 500-Torr Ar. The plume of ejected material is followed for several seconds after ablation using combined imaging and spectroscopy of Co atoms, C_2 and C_3 molecules, and clusters. The ablation plume expands in stages during the first 200 µs after ablation and displays a self-focusing behavior. Interaction of the plume with the background gas forms a vortex ring which segregates and confines the vaporized material within a $\sim 1\text{-cm}^3$ volume for several seconds. Using time-resolved spectroscopy and spectroscopic imaging, the time for conversion of atomic and molecular species to clusters was measured for both carbon (200 µs) and cobalt (2 ms) at 1000 °C. This rapid conversion of carbon to nanoparticles, combined with transmission electron microscopy analysis of the collected deposits, indicate that nanotube growth occurs over several seconds in a plume of mixed nanoparticles. By adjusting the time spent by the plume within the high-temperature zone using these in situ diagnostics, single-walled nanotubes of controlled (~ 100 nm) length were grown and the first estimate of a growth rate on single laser shots (0.2 µm/s) was obtained.

PACS: 42.62.Fi; 52.70.Kz; 81.05.Tp

Single-wall carbon nanotubes (SWNTs) exhibit remarkable electronic and structural properties which promise to revolutionize application areas from nanoscale electronics to ultralightweight structural materials [1]. In the six years since SWNTs were discovered [2, 3], research on their electronic properties and chemical functionalization has provided strong evidence that carbon nanotubes (in striking contrast to earlier fullerenes) will enable major advances in nanoscale electronic devices [4], micro electro mechanical systems (MEMS) [5, 6], biological probes [7], and field emission devices [8, 9]. Possibly of greatest significance, nanotubes may serve as molecular wires for input/output paths and interconnects between molecular electronic components or devices.

Recent experiments also show that SWNTs are highly thermally conductive [1], resistant to high temperatures and harsh chemicals [10], lightweight [11], incredibly strong in the axial direction (1-TPa Young's modulus) and resilient in the transverse [6], and their hollow structure makes them ideal for hydrogen storage [11] and drug delivery. These properties broaden the scope of nanotube applications into aerospace, transportation, and biotechnology.

However nanotube growth is not controlled or understood. In situ diagnostics have not been applied during growth, and therefore no mechanisms have been determined to control the atomic-scale structure (chirality) of nanotubes during synthesis. Since the electronic properties of chemically unmodified SWNTs are entirely determined by their chirality, electronic transport in as-grown nanotubes is currently uncontrolled. Furthermore, approaches for large-scale production of SWNTs for structural applications await measurements to determine their growth rate using current synthesis techniques, and methods to increase it toward the theoretical maximum.

Up until now, three principal methods have been used to synthesize carbon nanotubes. These include laser vaporization (LV) [12], dc-arc vaporization (AV) [2, 3, 13], and chemical vapor deposition (CVD) [14, 15]. Unlike CVD, both LV and AV now produce nearly exclusively SWNT. However, very little is known about where and when the SWNTs are formed in LV or AV growth chambers, the identity of the precursor species, and the growth rates.

Laser vaporization is arguably the best method to grow high-quality, high-purity SWNTs. As typically employed, a small amount of material ($\sim 10^{16}$ carbon atoms and $\sim 10^{14}$ metal catalyst atoms) is laser-vaporized inside a hot oven with gently flowing inert gas. On a single laser shot [16], this material self-assembles to form an astounding fraction of SWNTs (70–90 vol. % yield) under the correct conditions [17, 18]. Despite the wide range of metal catalyst nanoparticle diameters produced during pulsed-LV, only SWNTs are formed. Although SWNTs grow easily by nanosecond time-scale laser vaporization followed by annealing in a hot oven, they can also be grown by LV at room temperature where it appears that sufficient heating of the target or ejecta is accomplished by high-repetition-rate [19] or long-pulse (~ 10 ms) [20] lasers.

Pulsed-LV with ns lasers is especially amenable to diagnostic investigations. The vaporizing pulse lasts only ~ 10 ns and SWNT growth then can occur undisturbed from further excitation, even for single laser ablation events [16]. Recent spectroscopic measurements of the luminous laser plasma have been made for pulsed-LV at early times after Nd:YAG laser ablation ($< 200\,\mu s$) [21] and after long-pulse CO_2 laser ablation at room temperature [20]. However, these measurements were limited to times while the ablated material is still quite hot.

Recently laser-induced luminescence (LIL), gated intensified charge-coupled device (ICCD) imaging, and optical emission spectroscopy were applied to understand how nanoparticles form and grow in pulsed laser ablation plumes at room temperature [22–24]. In this study these techniques are applied to understand how SWNTs grow from laser-vaporized carbon and catalyst species under typical growth conditions at high temperatures.

1 Experimental

The SWNT growth setup in Fig. 1 was fashioned after that used by Guo et al. [12]. It consists of a quartz tube (2 in. diameter, 24 in. length) mounted inside a hinged tube furnace (12 in. length) operating at $1000\,°C$. The quartz tube was O-ring sealed to standard 4.5-in. Conflat vacuum components. The ablation and probe laser beams entered through the same Suprasil window which was mounted in a vacuum flange. Argon gas was introduced around this window, controlled at 100 sccm to maintain a 500 Torr pressure, and pumped out through a needle valve downstream of a brass, water-cooled collector which was inserted into the quartz tube and positioned just outside the oven.

A 1-in. diameter graphite target containing 1 at. % each of Ni (Alfa, 2.2–3.0 μm, 99.9%) and Co (Alfa, 1–6 μm, 99.8%) powders was prepared with the carbon cement (Dylon GC) procedure described in [12]. The target was screwed onto a 0.25-in. diameter graphite rod and was rotated during operation. This rod was mounted along the tube axis through a hole in the collector. The ablation laser (Nd:YAG, 8-ns FWHM pulse) beam was focused to a 1.6 mm-diameter, donut-shaped spot on the target. Both the 1.06-μm fundamental and the 532-nm 2nd-harmonic were used (with no time delay) to provide a total energy of 140 mJ at the target. An unfocused, time-delayed XeCl-laser pulse (308 nm, 30-ns FWHM, 20 mJ/cm^2) was used to induce luminescence in the ablation plume.

To permit imaging of the plume with a gated ICCD-camera system (Princeton Instruments, 5-ns minimum gate, 200–820 nm spectral range) the furnace was opened for ~ 3 seconds/per image. Alternatively, at each plume location lenses collected the plasma emission and/or laser-induced luminescence for optical emission spectroscopy using a 0.3-m spectrometer (Acton VM-503, resolution either 10 nm or 1.3 nm) with an intensified, gated diode array (Princeton Instrument IRY-700RB).

2 Single-wall carbon nanotube deposits

Carbon nanotubes were synthesized under a variety of laser repetition rates, flow conditions, target positions, and numbers of total shots on the target. Following each run, deposits were collected at various points in the reactor and analyzed by bright-field TEM for correlation with the transport dynamics observed during the run with time-resolved imaging and/or spectroscopy.

When the target was positioned $d = 21$ cm from the front of the furnace, $\sim 10\,\mu m$-long SWNT bundles comprised very high fractions of the deposit found downstream on the collec-

Fig. 2. a Field-emission SEM image of SWNT bundles, metal catalyst particles, and unconverted carbon soot produced by laser ablation of a C/Ni/Co target at $1000\,°C$. **b** TEM images of the raw soot collected: downstream on the collector (point 2, for $d = 21$ cm in Fig. 1), showing a very high fraction of SWNT bundles along with metal nanoparticles (*black dots*)
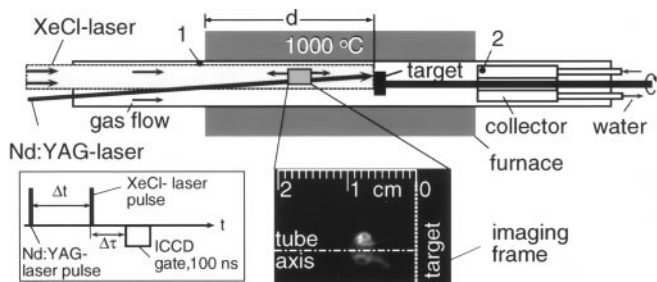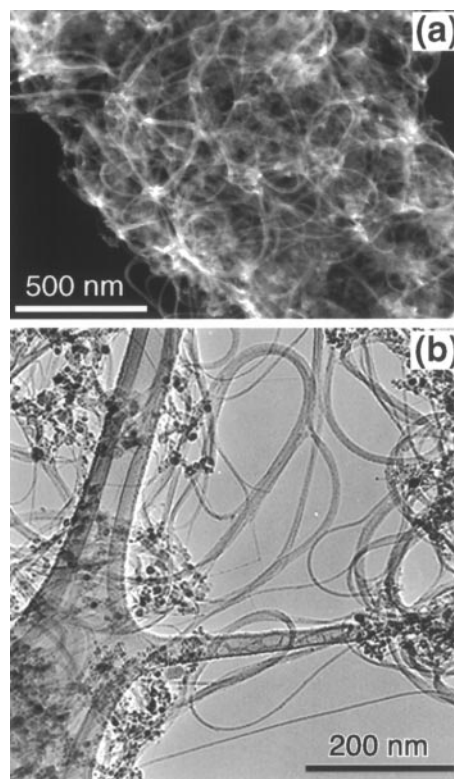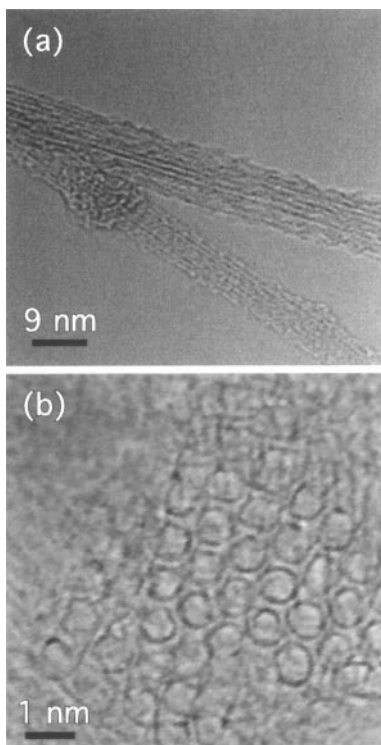

Fig. 1. Schematic of the $2''$-diameter quartz tube and hot furnace used for laser vaporization growth of SWNT with in situ LIL-imaging and spectroscopy diagnostics. Beam geometries and imageable area are indicated. The *black dots* and the *numbers* show the collection points of the ablated material: 1-upstream; 2-collector. The C/Ni/Co target was positioned at two distances, d, from the front of the furnace. The *inset on the left* shows the relative timing between ablation (Nd:YAG) and and LIL-probe (XeCl) laser pulses (Δt), and the ICCD gate delay after the XeCl laser, ($\Delta \tau$)

Fig. 3. a HRTEM images of bundles of SWNTs grown by laser ablation at 1000 °C. b A cross section of a nanotube bundle, revealing the shape and diameters of the hollow SWNT

tor. Figure 2a shows a field-emission SEM image of a deposit produced at a laser repetition rate of only 0.016 Hz. Over 90% of the deposit appears to consist of SWNT bundles as estimated from an areal analysis. Bright-field TEM images as in Fig. 2b show that metal catalyst nanoparticles and small amounts of amorphous carbon account for the rest of the deposit (as described in the literature) [12, 17, 18].

High-resolution scanning TEM images such as those in Fig. 3a confirm that the bundles consist of SWNTs. Cross-sectional images of the bundles permit an estimate of the nanotube diameters, as shown in Fig. 3b.

The ability to correlate these TEM and FESEM images of deposits with the plume transport dynamics (observed with in situ diagnostics, described below) permits conclusive assessment of the growth conditions. For example, the laser repetition rate for the deposit of Fig. 3 was chosen to ensure that the plume observed by imaging had completely cleared the growth chamber, so that the long nanotubes in Fig. 3 reflected SWNTs created on single laser shots.

3 Plume dynamics

To understand where and when nanotubes grow, ICCD imaging and spectroscopy of the C/Ni/Co plume were performed at different times after laser vaporization, Δt, spanning $20\,\mathrm{ns} \leq \Delta t \leq 3\,\mathrm{s}$. At early times, the ablated material is primarily in excited states and can be imaged directly from the plasma emission alone (without LIL excitation). Figure 4 compares the plume propagation at room temperature and at 1000 °C for $\Delta t \leq 200\,\mathrm{\mu s}$. In each case, the plume exhibits oscillations in both axial and

radial directions. Just after ablation, the plume expands both radially and axially and compresses the background gas. However, the initial kinetic energy of the plume contributes to its overexpansion into the background gas, and it expands past the position where the plume pressure equals that of the surrounding ambient. Recovering from this overexpansion, a backward motion is induced in the plume. In addition, a backward motion in the radial direction results in an axial focusing of the plume, as shown in Fig. 4.

The position of the leading edge of the plasma plumes is plotted versus time in Fig. 5. At 1000 °C, four axial oscillations, decaying in strength, are evident (at 40 ns, 200 ns, 2 μs, and 200 μs). At room temperature, three oscillations can be seen at 600 ns, 10 μs, and 300 μs. These oscillations result from the propagation of internal shock waves within the plume material, caused when the strong external shock wave is generated and detaches to propagate through the background gas. The plume material reflected from the contact
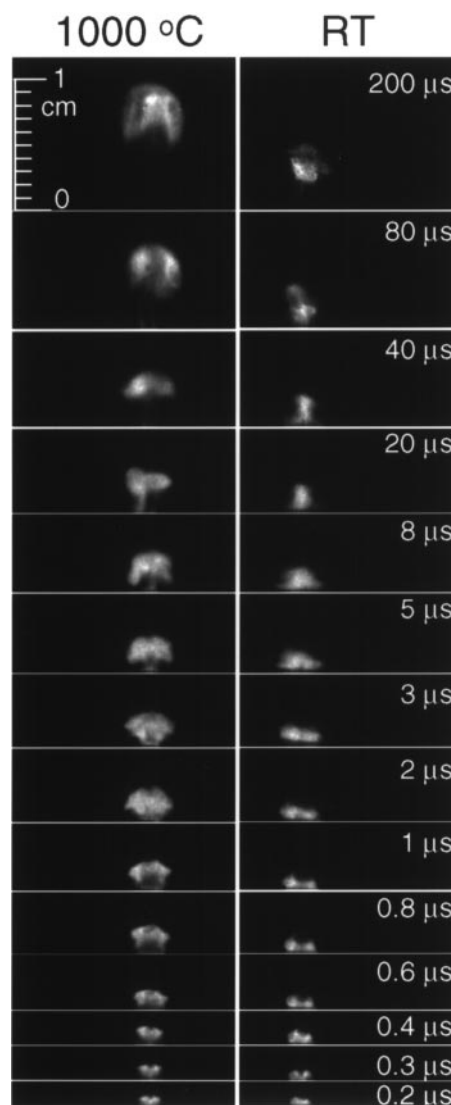

Fig. 4. ICCD images of the nascent plasma emission from the plume of vaporized C/Ni/Co target material at 1000 °C and at room temperature. The images show oscillations and self-focusing effects during the early dynamics of both plumes
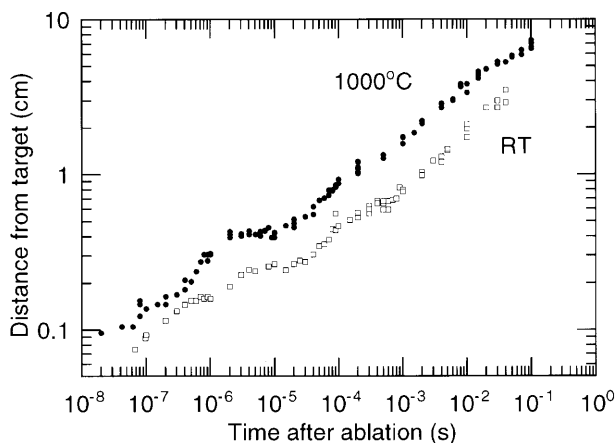
Fig. 5. Propagation of the leading edge of the ablation plumes shown in Fig. 4

surface between the plume and the background gas forms the internal shocks within the plume. These internal shocks serve to mix and additionally heat the atomic and molecular car-
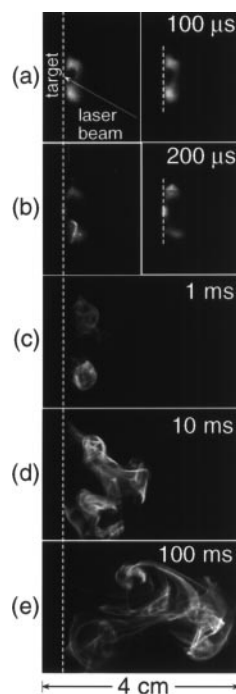

Fig. 6. a Laser-induced luminescence (LIL) images record the dynamics of the C/Ni/Co plume during SWNT synthesis. A Nd:YAG-laser vaporizes a C/Ni/Co target (right edge of figure) inside a 2-in. quartz tube at 1000 °C in 500-Torr Ar (flowing to the right at 100 sccm). Each image represents a different ablation event (100 ns gate width, opened $\Delta\tau = 100$ ns after the XeCl-laser pulse). **b** Enlarged view (2X) of the plume at 0.2 ms showing vortex ring. **c** LIL images at room temperature in 500-Torr Ar. **d** Integrated total emission from LIL-images acquired at the indicated times at 1000 °C and room temperature

Fig. 7a–d. Images of Rayleigh-scattered (RS) light (308 nm XeCl-laser, 26 ns, 20 mJ/cm^2) and plasma emission from a carbon vapor plume generated by KrF-laser (248 nm, 28 ns FWHM, 7 J/cm^2) ablation of a pyrolitic graphite target into 300-Torr Ar at room temperature. The onset of clustering can be gauged by comparing **a–b** RS (*left*) vs. plasma emission images (*right*). **c–d** RS images at later times show the highly turbulent motion of plume material and its confinement within thin sheets
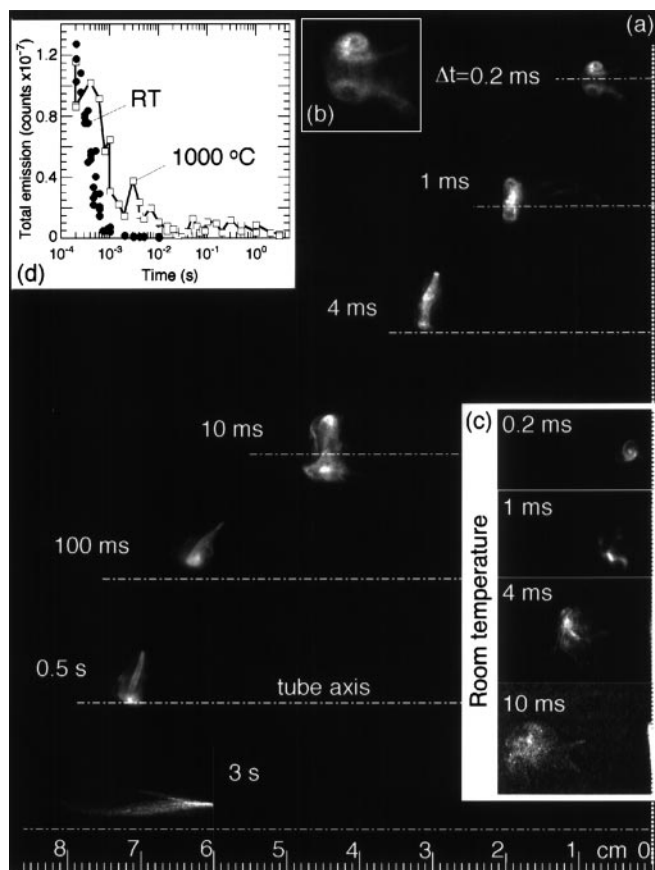
bon and the catalyst species within the plume. This oscillatory behavior of laser plasmas propagating into background gases has been observed before [25, 26] and has been described theoretically [27].

Following these plume oscillations [25, 26] during $\Delta t \leq 0.2$ ms, the ablated material is segregated into a vortex ring [27, 28] (or "smoke ring") [22] shown at $\Delta t = 0.2$ ms in Fig. 6a,b. This vortex ring is generated because of the viscous interaction between the plume and the background gas. Vortex formation efficiently mixes the ablated species with the background gas, promoting clustering of the plume species through three-body collisions. Then the vortex motion efficiently traps aggregated nanoparticles in a confined volume for long times (~ 3 s within ~ 1 cm^3 in this study) as shown in Fig. 6a.

The leading edge of the plume in Fig. 6a propagates with velocities of: 10^3 cm/s between $200\,\mu s < \Delta t < 2$ ms; 50 cm/s for 10 ms $< \Delta t < 50$ ms; and 6 cm/s during 30 ms $< \Delta t < 200$ ms. After $\Delta t = 2$ s the plume stops moving upstream, and the plane of the vortex ring tilts toward the tube axis, possibly due to flow currents or thermophoretic forces. The plume is then dragged by the gas flow back to the collector with an estimated flow velocity of 0.6 cm/s. Finally, nanotubes and unconverted soot deposit on the cool collector surface by thermophoresis [24].

At room temperature the plume dynamics at later times are completely different. As shown in Fig. 6c, the plume propagates slower in the axial direction and the motion of the material within the plume is highly turbulent. This turbulent behavior can be seen more explicitly using Rayleigh scatter-

ing from the nanoparticles which form during the cooling of the laser plasma in the background gas.

Rayleigh-scattering images of the plume evolution from a pure graphite target after KrF-laser ablation into 300-Torr Ar, are shown in Fig. 7. By comparing images of the plasma with and without secondary laser-irradiation, the emergence of Rayleigh scattering can be used to estimate the onset of plume condensation into nanoparticles [24]. Under these conditions, this time is estimated at 150 μs after ablation from these images. The highly turbulent behavior evident in the images likely results from the higher background gas density and smaller gas viscosity compared to those at 1000 °C. Despite the plume expansion, the ablated material remains confined to a relatively small volume within the thin sheets of multiple vortices.

4 Plume spectroscopy

Once the plume was located with ICCD imaging, several spectroscopic techniques were applied to probe its composition, including: optical emission spectroscopy (OES) from excited states in the plasma; optical absorption spectroscopy (OAS) and laser-induced fluorescence (LIF) from ground-state atoms and molecules; laser-induced blackbody emission and Rayleigh scattering from clusters, nanoparticles, and nanotubes.

To understand the nature of the carbon species ejected from the target, OAS was performed in vacuum [29]. Figure 8a shows a low-resolution (2.6 nm) absorption spectrum of the plume from a pure graphite target. The spectrum is dominated by C_3 absorption via $A\,^1\Pi_u \leftarrow X\,^1\Sigma_g$ and C_2 absorption: in the $\Delta v = -2, -1, 0$, and $+1$ sequences of the Swan $d\,^3\Pi_g \leftarrow a\,^3\Pi_u$ system; and the $\Delta v = 0$ sequence of the Mulliken $D\,^1\Sigma_u{}^+ \leftarrow X\,^1\Sigma_g{}^+$ system. The dominance of C_3 as the principal component of the plume is consistent with mass spectrometric measurements under the same conditions which show that the composition of the plume is primarily C_3, C_2, and C with very few higher order clusters (intensity ratio, $C:C_2:C_3C_4:C_5 = 56:35:100:2.5:1.6$) [30].

Ground-state C_3 in the plume was probed by laser-induced fluorescence with a 308-nm XeCl laser. Figure 8b shows the LIF spectrum of vaporized graphite in vacuum, displaying predominantly $C_3\ A\,^1\Pi_u \rightarrow X\,^1\Sigma_g$ emission (resolution 10 nm). In addition, weak $\Delta v = 0\ C_2$ Swan $d\,^3\Pi_g \rightarrow a\,^3\Pi_u$ emission can be observed at 516 nm. The XeCl laser can also excite vibronically induced absorption of C_3 via $^1\Pi_g$ and/or $^1\Delta_u \leftarrow X\,^1\Sigma_g$ [31].

In addition, the XeCl laser can induce emission from atomic Co (via $a\,^4F_J \leftarrow y\,^4G_J{}^o$) and from atomic Ni (via $a\,^3D_1 \leftarrow y\,^3D_2{}^o$). It therefore serves as an excellent probe of the ground state atoms and molecules in the plume, both for laser-induced luminescence (LIL) spectroscopy, and spectroscopic imaging (see Sect. 5) of the separate components.

From sets of images as in Fig. 6, both OES and LIL-spectra were acquired at 1000 °C and at room temperature (RT). Figures 9 and 10 present a short summary of these spectra, with nascent plasma emission plotted along with the LIL-emission whenever both could be detected. At early times in the plume expansion, close to the target while the plasma is very hot, the plume species are primarily electronically excited and this emission from
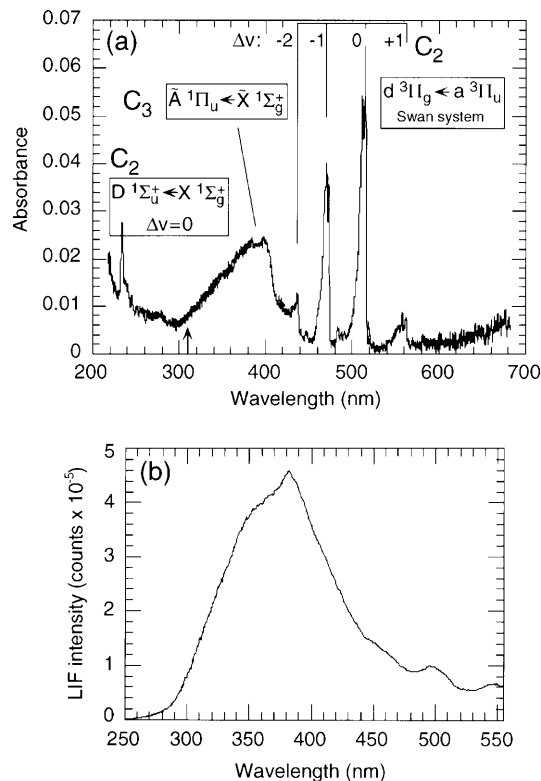

Fig. 8. a Gas-phase absorption spectrum of the carbon vapor plume generated by KrF laser (1.6 J/cm²) ablation of a pyrolitic graphite target into vacuum. The spectrum was acquired $d = 0.5$ cm from the target surface, with a 400-ns gate width beginning 1 μs after the KrF-laser pulse. **b** LIF (XeCl-laser, 20 mJ/cm²)-spectrum of C_3 in the carbon vapor plume generated by KrF-laser in vacuum

excited states dominates any laser-induced luminescence (from the ground states) both at 1000 °C (Fig. 9) and at RT (Fig. 10). Bright nascent emission from C_2 ($d\,^3\Pi_g \rightarrow a\,^3\Pi_u$, Swan system) and C_3 ($A\,^1\Pi_u \rightarrow X\,^1\Sigma_g$) dominate at these times. As the plasma expands, cools, and recombines, the ground states become populated, and LIL-emission emerges to compete with the nascent plasma emission. At 1000 °C, LIL from atomic Co in the 320–380 nm range (see high-resolution spectrum in Fig. 9) is clearly visible. Finally, the nascent plasma emission completely disappears, and only LIL from ground states remains. From previous measurements of clustering in laser plasmas expanding into background gases, this disappearance of the nascent plasma emission usually signals the onset of nanoparticle formation [22–24].

Laser-induced blackbody radiation can be used to signal the presence of carbon clusters [32], nanoparticles [33], and nanotubes. The intensity of this blackbody emission, I, is defined by

$$I = Ar^3(T_0 + \Delta T)^5 , \qquad (1)$$

where T_0 is the initial temperature of the cluster, ΔT is the temperature increase due to laser heating, A is a constant, and r is the cluster radius.

Induced blackbody radiation becomes observable for $\Delta t > 200$ μs at 1000 °C (Fig. 9) and for $\Delta t > 50$ μs at room temperature (Fig. 10), coincident with the disappearance
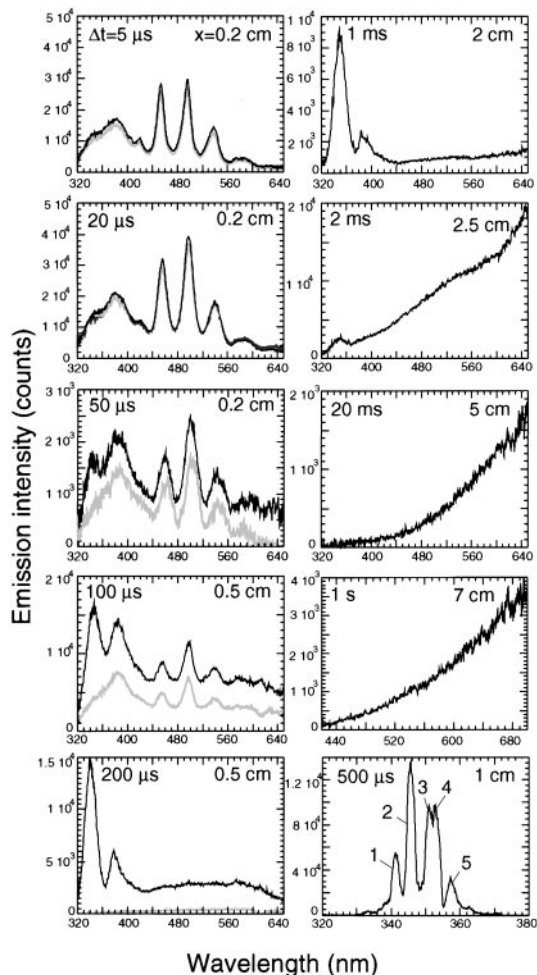
Fig. 9. Plasma emission (*lighter curve*) and laser-induced luminescence (*black curve*) spectra measured at different time delays after the ablation laser pulse, Δt, and distances, x, from the target at 1000 °C during SWNT synthesis: Acquisition times of 100 ns (for $\Delta t \leq 1$ ms) and 3.5 µs (for $\Delta t > 1$ ms) began 50 ns after the XeCl-laser pulse. Higher resolution (1.3-nm) LIL-spectrum in the 320–380 nm region (*bottom, right*) show the following transitions of atomic Co: (1) $b\,^4F_{7/2}$-$y\,^2G_{9/2}^0$ at 341.23 nm (2) $b\,^4F_{9/2}$-$y\,^4G_{11/2}^0$ at 345.35 nm (3) $b\,^4F_{5/2}$-$y\,^4G_{7/2}^0$ at 350.98 nm (4) $b\,^4F_{7/2}$-$y\,^4G_{9/2}^0$ at 352.98 nm, and (5) $b\,^4F_{5/2}$-$y\,^4D_{5/2}^0$ at 357.50 nm

of the C_2 and C_3 bands in both the plasma-emission and the laser-induced spectra for $\Delta t > 200$ µs at 1000 °C (and $\Delta t > 50$ µs at room temperature). From these two coincident measurements, we conclude that the carbon in the plume has all converted into clusters or larger aggregates by these times.

However, the atomic Co in the plume remains in atomic form long after the atomic and molecular carbon has disappeared. Integrating the emission in the 320–380 nm range from the LIL-spectra, the ground-state Co population is observed to peak at $\Delta t = 0.8$ ms and drop by an order of magnitude by $\Delta t = 2$ ms, permitting estimates of the Co clustering time of ~ 2 ms at 1000 °C (~ 1 ms at room temperature). A similar estimation for the Co clustering time can be performed using spectroscopic imaging of the Co vapor plume (see Fig. 11c in Sect. 5).

Blackbody radiation remains the only feature of the spectra taken for $\Delta t > 2$ ms at 1000 °C (and images, see Fig. 6d). At room temperature the laser-induced blackbody radiation
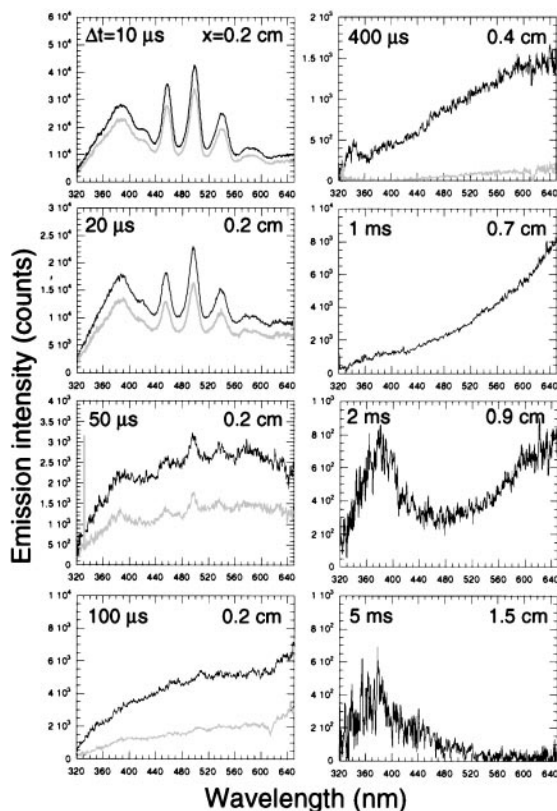

Fig. 10. Plasma emission (*lighter curve*) and laser-induced luminescence (*black curve*) spectra measured at room temperature at different time delays after the ablation laser pulse, Δt, and distances, x, from the target at (100 ns acquisition times began 35–75 ns after the XeCl-laser pulse)

disappears rapidly ($\Delta t \sim 5$ ms) for the low XeCl-laser intensity employed here (chosen for use at $T_0 = 1000$ °C in (1)). The last recognizable feature of the spectrum (see 5 ms image of Fig. 10) is a broad band at 380 nm, which is currently unidentified.

Hot particulates from the target would be easily imaged via their blackbody emission [34] or by Rayleigh scattering. It is important to note that we observed very few particulate ejecta for the properly outgassed, hard, Dylon-fabricated targets used in this study.

5 Spectroscopic imaging

Once sharp spectral features have been identified throughout a set of spectroscopic data (such as those described in Sect. 4), optical filters can be used in conjunction with ICCD imaging to selectively image different constituents of the plume. Here, the 320–380 nm spectral region was imaged at 1000 °C to locate the ground-state atomic Co in the plume.

Figure 11a,b shows these images along with corresponding images from a pure carbon plume (to assess the extent of blackbody emission from carbon species in the same spectral region). The total integrated luminescence from both sets of images is plotted in Fig. 11c. Again, the ground-state atomic Co population is observed to rise (due to population of the ground states via cooling of the hot plasma) and then decay as these atoms become incorporated in clusters. As in Fig. 6, the
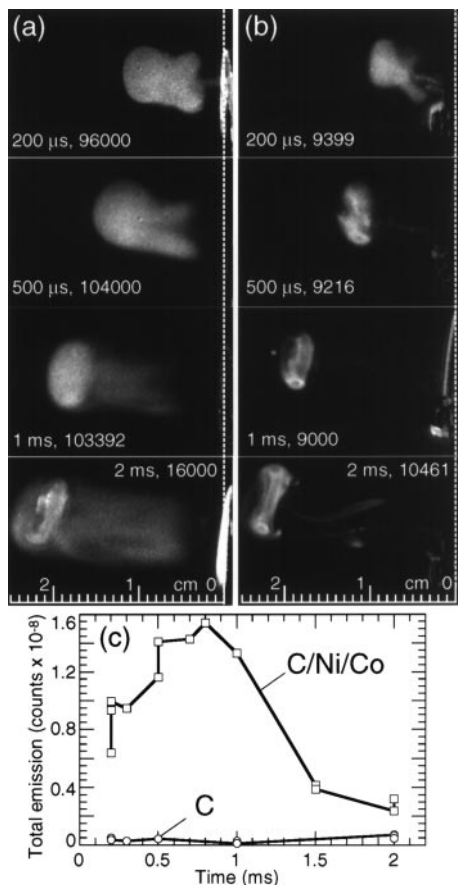
Fig. 11a–c. Selective imaging in the 320–380 nm spectral range at high temperature in 500-Torr Ar (100 ns gate width, $\Delta\tau = 0$, peak image intensities listed) **a** to locate ground-state atomic Co in the plume under conditions for SWNT synthesis using a graphite/Ni/Co target, and **b** to locate carbon species in the same region using a pure pyrolitic graphite target. **c** Total emission intensities from sets of images as shown in **a**, **b** compare the ground-state atomic Co temporal history (from C/Ni/Co target) and the background blackbody emission from carbon species (from C target) in the same spectral region

carbon in the plume clusters much more quickly and forms a vortex ring.

Further evidence of the sequential condensation of carbon and cobalt into clusters is the relatively uniform spatial distribution of atomic Co in the plume for $\Delta t < 2$ ms compared to the vorticity of the clustered carbon material (compare Fig. 11a,b). We believe that the higher diffusivity of the atomic Co effectively competes with the hydrodynamic trapping within the vortex during this time. Only the leading edge of the atomic-Co plume overlaps the carbon clusters during the condensation of the Co atoms. Assuming that Co clustering initiates nanotube formation, it appears that nanotubes grow from a feedstock of aggregated nanoparticles during seconds of time, confined first within the vortex ring and then by thermophoresis and fluid flow in the quartz tube.

6 Controlled SWNT growth with in situ diagnostics

In order to check this conclusion and estimate the growth rate, the target was positioned closer to the front furnace edge ($d = 12.5$ cm in Fig. 1) such that the plume spent only ~ 0.5 s

within the hot zone before exiting the furnace in the upstream direction (as shown in Fig. 12a). From estimates of heat transfer coefficients and the thermal diffusivity of the gas (convection currents were not considered) the thermal gradient near the upstream edge of the furnace was estimated to extend ~ 5 cm into the tube ($d > 7$ cm in Fig. 12a). Thermophoresis is a powerful driving force for gas-suspended nanoparticles, driving them toward cooler regions of the growth chamber (and permitting capture of the nanomaterials on the collector) [24]. The intention in this experiment was to utilize the natural plume velocity in the upstream direction (determined from Fig. 6) to drive the plume into the region of the thermal gradient near the upstream edge of the furnace. LIL-ICCD imaging recorded the plume dynamics from ablation to deposition.

The plume motion in Fig. 12a is quite similar to that of Fig. 6 for $\Delta t < 100$ ms. However, for $\Delta t > 100$ ms the plume propagation changes dramatically, i.e. the plane of the ring vortex tilts relative to the tube axis and the ring elongates along this axis. Between 0.5–0.7 s the plume exits the furnace in this tilted orientation to deposit onto the upper surface of the quartz tube (at point 1 in Fig. 1).

A transmission electron microscopy (TEM) image of this deposit is shown in Fig. 12b. The collected material consists of aggregated carbon and metal-catalyst nanoparticles, and thin SWNT bundles of only ~ 100 nm length. The relative yield of the carbon particles is larger than the yield of the carbon nanotubes which clearly shows that the time spent by the plume in the hot zone (~ 0.5 s) was not sufficient to convert all of the carbon material into nanotubes. This combined
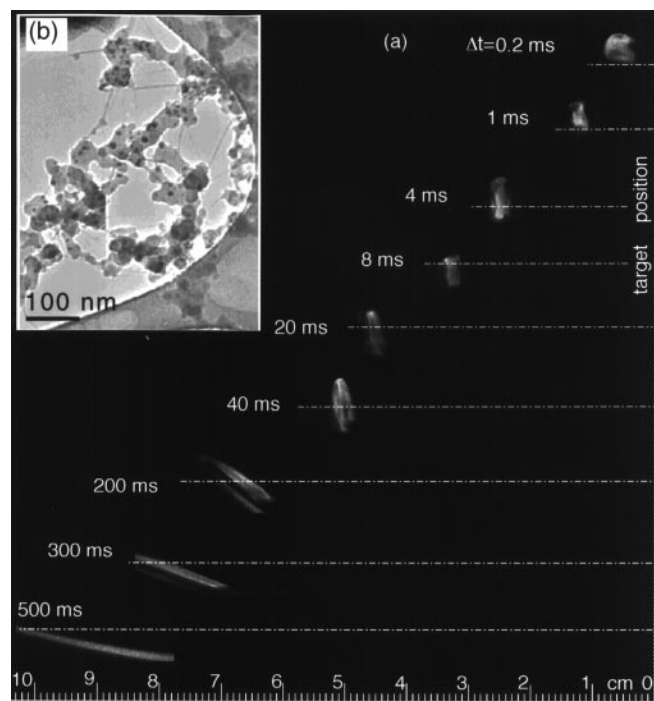

Fig. 12. **a** Laser-induced luminescence (LIL) images of the C/Ni/Co plume during synthesis of SWNT with controlled growth times of ~ 0.5 s. The target is positioned at $d = 12.5$ cm in Fig. 1. **b** Corresponding deposit collected at point 1 in Fig. 1, showing short (~ 100 nm) SWNT in the early stages of growth

imaging and TEM analysis permits the average growth rate at 1000 °C to be estimated at ∼ 0.2 µm/s.

7 Conclusions

In summary, we have used laser-induced imaging and spectroscopy diagnostic techniques, along with ex situ TEM, to determine that single-walled carbon nanotubes form over several seconds inside the hot furnace after laser vaporization. Size-controlled SWNTs were formed in short 100-nm lengths by controlling the growth time with these diagnostics to ∼ 0.5 s, yielding 0.2 µm/s for the first estimate of the SWNT growth rate by LV. The spectroscopy at early times after laser ablation indicates that the plume initially consists of atomic and molecular species, with no evidence of hot molten particulates which were recently suggested as the primary ejecta [35]. Condensation of carbon occurs within 0.2 ms after ablation, whereas atomic Co condenses much later (between 1.5 and 2 ms) at 1000 °C. The nanotubes grow within a vortex ring which trap clusters and aggregates within a ∼ 1-cm^3 volume during very long periods of time (∼ 3 s). Assuming that metal catalyst clusters are required before carbon nanotube growth begins, we conclude that feedstock for nanotube growth is this mixture of carbon and metal catalyst nanoparticles. It is quite possible that the carbon clusters serve as the condensation centers for the metal clusters, and mixed carbon–catalyst alloy clusters are produced. Finally, we produced high-purity SWNT deposits with laser repetition rates as low as 0.016 Hz. Through these images of the growth process, we conclude that long (∼ 10 µm) SWNTs can form from the small amount of material vaporized in a single-laser shot, a remarkable feat of self-assembly.

References

1. B.I. Yakobson, R.E. Smalley: Am. Sci. **85**, 324 (1997)
2. S. Iijima, T. Ichihashi: Nature **363**, 603 (1993)
3. D.S. Bethune, C.H. Kiang, M.S. de Vries, G. Gorman, R. Savoy, J. Vazquez, R. Beyers: Nature **363**, 605 (1993)
4. Ph. Avouris, T. Hertel, R. Martel, T. Schmidt, H.R. Shea, R.E. Walkup: Appl. Surf. Sci. **141**, 201 (1999)
5. R.H. Baughman, C. Cui, A.A. Zakhidov, Z. Iqbal, J.N. Barisci, G.M. Spinks, G.G. Wallace, A. Mazzoldi, D. De Rossi, A.G. Rinzler, O. Jaschinski, S. Roth, M. Kertesz: Science **284**, 1340 (1999)
6. P. Poncharal, Z.L. Wang, D. Ugarte, W.A. de Heer: Science **283**, 1513 (1999)
7. S.S. Wong, E. Joselevich, A.T. Woolley, C.L. Cheung, C.M. Lieber: Nature **394**, 52 (1998)
8. H. Schmid, H.-W. Fink: Appl. Phys. Lett. **70**, 2679 (1997)
9. J. Li, C. Papadopoulos, J.M. Xu, M. Moskovits: Appl. Phys. Lett. **75**, 367 (1999)
10. J. Liu, A.G. Rinzler, H. Dai, J.H. Hafner, R.K. Bradley, P.J. Boul, A. Lu, T. Iverson, K. Shelimov, C.B. Huffman, F. Rodriguez-Macias, Y.-S. Shon, T.R. Lee, D.T. Colbert, R.E. Smalley: Science **280**, 1253 (1998)
11. Y. Ye, C.C. Ahn, C. Witham, B. Fultz, J. Liu, A.G. Rinzler, D. Colbert, K.A. Smith, R.E. Smalley: Appl. Phys. Lett. **74**, 2307 (1999)
12. T. Guo, P. Nikolaev, A. Thess, D.T. Colbert, R.E. Smalley: Chem. Phys. Lett. **236**, 419 (1995)
13. C. Journet, W.K. Maser, P. Bernier, A. Loiseau, M. Lamy de la Chapelle, S. Lefrant, P. Deniard, R. Lee, J.E. Fisher: Nature **388**, 756 (1997)
14. H.M. Cheng, F. Li, G. Su, H.Y. Pan, L.L. He, X. Sun, M.S. Dresselhaus: Appl. Phys. Lett. **72**, 3282 (1998)
15. B.C. Satiskumar, A. Govindaraj, R. Sen, C.N.R. Rao: Chem. Phys. Lett. **293**, 47 (1998)
16. M. Yudasaka, T. Ichihashi, T. Komatsu, S. Iijima: Chem. Phys. Lett. **299**, 91 (1999)
17. A. Thess, R. Lee, P. Nikolaev, H. Dai, P. Petit, J. Robert, C. Xu, Y.H. Lee, S.G. Kim, A.G. Rinzler, D.T. Colbert, G.E. Scuseria, D. Tomanek, J.E. Fisher, R.E. Smalley: Science **273**, 483 (1996)
18. A.G. Rinzler, J. Liu, H. Dai, P. Nikolaev, C.B. Huffman, F.J. Rodriguez-Macias, P.J. Boul, A.H. Lu, D. Heymann, D.T. Colbert, R.S. Lee, J.E. Fisher, A.M. Rao, P.C. Eklund, R.E. Smalley: Appl. Phys. A **67**, 29 (1998)
19. A.C. Dillon, P.A. Parilla, K.M. Jones, G. Riker, M.J. Heben: In *Advances in Laser Ablation of Materials*, ed. by R.K. Singh, D.H. Lowndes, D.B. Chrisey, E. Fogarassy, J. Narayan (Warrendale, PA, USA: Mater. Res. Soc. 1998) pp. 403–408
20. F. Kokai, K. Takahashi, M. Yudasaka, R. Yamada, T. Ichihashi, S. Iijima: J. Phys. Chem. B **103**, 4346 (1999)
21. S. Arepalli, C.D. Scott: Chem. Phys. Lett. **302**, 139 (1999)
22. D.B. Geohegan, A.A. Puretzky, G. Duscher, S.J. Pennycook: Appl. Phys. Lett. **72**, 2987 (1998)
23. D.B. Geohegan, A.A. Puretzky, G. Duscher, S.J. Pennycook: Appl. Phys. Lett. **73**, 438 (1998)
24. D.B. Geohegan, A.A. Puretzky, D.J. Rader: Appl. Phys. Lett. **74**, 3788 (1999)
25. D.B. Geohegan, A.A. Puretzky, R.L. Hettich, X.-Y. Zheng, R.E. Haufler, R.N. Compton: In Advanced Materials '93, IV/Laser and Ion Beam Modification of Materials, ed. by I. Yamada, et al., Trans. Mater. Res. Soc. Jpn. **17**, 349 (1994)
26. Images also available online at www.ornl.gov/∼odg
27. A.V. Bulgakov, N.M. Bulgakova: J. Phys. D: Appl. Phys. **31**, 693 (1998)
28. F. Garrelie, C. Champeaux, A. Catherinot: Appl. Phys. A **69**, 45 (1999)
29. D.B. Geohegan, A.A. Puretzky: Appl. Phys. Lett. **67**, 197 (1995)
30. D. Krajnovich: J. Chem. Phys **102**, 726 (1995)
31. E.A. Rohlfing: J. Chem. Phys. **91**, 4531 (1989)
32. D.B. Geohegan, A.A. Puretzky: Mater. Res. Symp. Proc. **397**, 55 (1996)
33. E.A. Rohlfing: J. Chem. Phys. **89**, 6103 (1988)
34. D.B. Geohegan: Appl. Phys. Lett. **62**, 1463 (1993)
35. M. Yudasaka, R. Yamada, N. Sensui, T. Wilkins, T. Ichihashi, S. Iijima: J. Phys. Chem. B **103**, 6224 (1999)